Acta Pharmaceutica Sinica B 2025;15(10):4995−5009

Chinese Pharmaceutical Association
Institute of Materia Medica, Chinese Academy of Medical Sciences

Acta Pharmaceutica Sinica B

www.elsevier.com/locate/apsb
www.sciencedirect.com

ORIGINAL ARTICLE

A dual-targeting peptide−drug conjugate based on CXCR4 and FOLR1 inhibits triple-negative breast cancer

Kun Wang[a,†], Cong Wang[b,†], Hange Yang[b,†], Gong Chen[b,†], Ke Wang[b], Peihong Ji[b], Xudong Sun[b], Xuegong Fan[b], Jie Ma[c], Zhencun Cui[d], Xingkai Wang[a], Hao Tian[a], Dengfu Wu[a], Lu Wang[c], Zhimin Wang[e], Jiangyan Liu[d], Juan Yi[b,*], Kuan Hu[a,*], Hailong Zhang[b,*], Rui Wang[a,b,*]

[a]*State Key Laboratory of Bioactive Substance and Function of Natural Medicines, Institute of Materia Medica, Chinese Academy of Medical Sciences and Peking Union Medical College, Beijing 100000, China*
[b]*Key Laboratory of Preclinical Study for New Drugs of Gansu Province, School of Basic Medical Sciences & Research Unit of Peptide Science, Chinese Academy of Medical Sciences, 2019RU066, Lanzhou University, Lanzhou 730000, China*
[c]*Center of Cyclotron and PET Radiopharmaceuticals, Department of Nuclear Medicine & Key Laboratory of Basic and Translational Research on Radiopharmaceuticals, the First Affiliated Hospital of Jinan University, Guangzhou 510630, China*
[d]*Department of Nuclear Medicine, Second Hospital of Lanzhou University, Lanzhou 730000, China*
[e]*PET/CT Center of Gansu Provincial Hospital, Lanzhou 730000, China*

Received 17 January 2025; received in revised form 1 April 2025; accepted 10 June 2025

KEY WORDS

Triple-negative breast cancer;
Peptide−drug conjugate;
CXCR4;

Abstract Triple-negative breast cancer is therapeutically challenging due to the low expression of tumor markers and 'cold' tumor immunosuppressive microenvironment. Here, we present a dual-targeting peptide−drug conjugate (PDC) for tumor inhibition. Our PDC efficiently and selectively delivers cytotoxic Monomethyl Auristatin E (MMAE) into tumor cells *via* C−X−C chemokine receptor type 4 (CXCR4) and folate receptor 1 (FOLR1) for synergistic inhibition of growth and metastasis. Our results

This article is part of a special issue entitled: Targeted Radiopharmaceuticals published in Acta Pharmaceutica Sinica B.
*Corresponding authors.
E-mail addresses: yij@lzu.edu.cn (Juan Yi), hukuan@imm.ac.cn (Kuan Hu), zhanghailong@lzu.edu.cn (Hailong Zhang), wangrui@lzu.edu.cn (Rui Wang).
[†]These authors made equal contributions to this work.
Peer review under the responsibility of Chinese Pharmaceutical Association and Institute of Materia Medica, Chinese Academy of Medical Sciences.

https://doi.org/10.1016/j.apsb.2025.06.012

FOLR1;
Antitumor;
Monomethyl auristatin E;
Radiotherapy;
Tumor microenvironment

show that the dual-targeting PDC has potent antitumor activity in cultured human cells and several murine transplanted tumor models without apparent toxicity. The combination of dual-targeting PDC and radiotherapy modulates the tumor immunosuppressive microenvironment by increasing $CD8^+$ T cell infiltration and attenuating the proportion of myeloid-derived suppressor and regulatory T cells. Therefore, our dual-targeting PDC represents a promising new strategy for cancer therapy that rebalances the immune system and promotes tumor regression.

1. Introduction

The incidence of breast cancer has increased over the past four decades, and it is currently the second most widespread and fatal malignancy among women[1−4]. Triple-negative breast cancer (TNBC), characterized by a lack of estrogen receptor, progesterone receptor, and human epidermal growth factor receptor 2 expressions, is the most aggressive subtype[5−8]. Many effective targeted therapies have been developed for breast cancer, including monoclonal antibodies, tyrosine kinase inhibitors, antibody−drug conjugates (ADCs), bispecific antibodies, immune system-targeting drugs, cell therapy, and targeted protein degraders[9]. However, these treatments have limited efficacy against TNBC due to the lack of cell surface markers, malignancy, heterogeneity, and drug resistance[10−12]. Up to now, only three conjugated drugs have been approved for the treatment of TNBC, including a TROP2-targeting ADC (Sacituzumab govitecan). Therefore, it is crucial to identify available targets and drug combination strategies for more effective TNBC therapy[13−15].

Peptide−drug conjugates (PDCs) are an emerging targeted therapy that is similar to ADCs, with core advantages that include enhanced cell permeability and improved tumor targeting. In recent years, drug conjugates, including ADCs and PDCs, have displayed exciting therapeutic results in clinical and preclinical studies[16,17]. Compared to ADCs, PDCs: 1) are smaller molecular weight, allowing them to more easily penetrate the tumor stroma; 2) are more easily cleared by the kidney so that there is less toxicity to the bone marrow and liver[18]; 3) have less immunogenic effects; 4) are more rapidly synthesized, with a capacity for site-specific labeling of peptides[19]. Since 2018, when the FDA approved the first PDC (^{177}Lu-DOTATATE) for the treatment of gastroenteropancreatic neuroendocrine tumors[20], more than 100 PDCs have been evaluated for clinical development for tumor treatment and diagnosis.

The expression of CXCR4, a cell surface G-protein-coupled receptor, is positively correlated with the poor prognosis of melanoma and glioma[21,22]. When CXCR4 binds to its endogenous ligand CXCL12, it induces tumor metastasis[23] and inhibits T cell-mediated antitumor immunity[24]. In recent years, high expression of CXCR4 has been found in a variety of solid tumors, including metastatic TNBC[25−29]. T140, a naturally derived CXCR4 antagonist peptide, binds to CXCR4, enters cells, and recruits β-arrestin, causing a blockade of the interaction between CXCL12 and CXCR4 and inhibition of tumor metastasis and growth; its derivative Motixafortide (BKT140) was approved by the FDA for oncology treatment in 2023[30−32].

Similar to CXCR4, folate receptor 1 (FOLR1) is highly expressed in TNBC and a variety of other tumors. Its ligand folate (FA) can specifically target and inhibit the proliferation and migration of breast cancer cells[33,34]. Over the last decade, FA has been used as a targeted ligand to construct nanomedicines for the treatment and diagnosis of breast cancer[35−37], suggesting that FOLR1 may comprise an additional helpful target for the development of TNBC therapy.

Chemoradiotherapy has been clinically proven to achieve satisfactory results in the treatment of solid tumors by combining independent tumor-killing mechanisms that reduce drug resistance with chemotherapy by increasing tumor sensitivity to radiotherapy[38−40]. Although combination therapy improves survival, the systemic distribution of chemotherapy causes damage to normal tissues. Therefore, we speculated that drug conjugates might synergistically enhance the efficacy of TNBC chemotherapy by providing targeting capabilities.

In the present study, we constructed a dual-targeting PDC composed of T140, FA, the Val-Cit-PABC linker, and the tubulin polymerization inhibitor monomethyl auristatin (MMAE) for selective inhibition of tumor growth and metastasis. Additionally, we synthesized a dual-targeting peptide-radionuclide conjugate (PRC) based on CXCR4 and FOLR1 and used it for *in vivo* imaging of tumors. For the 4T1 TNBC tumor model, the combination of PDC and radiation effectively inhibited tumor growth and potentiated tumor immunity by increasing T lymphocyte infiltration and reducing the proportion of immunosuppressive cells. Thus, our dual-targeting PDC can efficiently target tumors and enhance tumor immunity.

2. Materials and methods

2.1. Cells and reagents

For biological experiments, MCF-7, MDA-MB-231, MCF-10A, L-02, Daudi, 4T1, MC38, CT26, and B16F10 cells were acquired from the National Collection of Authenticated Cell Cultures (Shanghai, China). 4T1-luci cells were a gift from Juan Yi, Lanzhou University, China. MCF-7, MDA-MB-231, MCF-10A, B16F10 cells were cultured in DMEM (BasalMedia Technologies Co., Ltd., Shanghai, China) supplemented 10% FBS (ABW, NOVA Medical Science and Technology Co., Ltd., Shanghai, China) and 1% penicillin−streptomycin solution (Labgic Technology Co., Ltd., Beijing, China). L-02, Daudi, 4T1, 4T1-luci, MC38, CT26 cells were cultured in RPMI-1640 media (BasalMedia Technologies Co., Ltd., Shanghai, China) supplemented with 10% FBS (ABW, NOVA Medical Science and Technology Co., Ltd., Shanghai, China) and 1% penicillin−streptomycin solution (Labgic Technology Co., Ltd., Beijing, China). On receipt, each cell line was expanded, cryopreserved as low passage stocks, and routinely tested for mycoplasma. The

cells were grown with 5% CO_2 at 37 °C. Reagents were purchased from Energy chemical and Bidepharm, and were used without further purification.

2.2. Synthesis of TM1, TM2 and TFM

Compound **1** (500 mg, 1.05 mmol) and compound **2** (384 mg, 3.15 mmol) were dissolved in 10 mL *N*,*N*-dimethylformamide (DMF), followed by *N*,*N*-diisopropylethylamine (DIEA) (30 mg, 0.231 mmol), and stirred at room temperature for 5 h. The solution was concentrated and then precipitated by adding ethyl acetate (40 mL). The mixture was washed with ethyl acetate to obtain compound **3** (620 mg, 0.97 mmol).

Compound **3** (267 mg, 0.42 mmol), compound **4** (300 mg, 0.42 mmol), and 1-hydroxybenzotriazole (HOBT) (25 mg, 0.1878 mmol) were dissolved in 6 mL DMF, followed by pyridine (883 mg, 11.18 mmol) and stirred overnight. The solution was concentrated and purified by HPLC using 20%−80% acetonitrile in water and 0.1% trifluoroacetic acid (TFA) over 60 min at 6 mL/min flow rate. The purified product was dried using lyophilization to obtain Alkynyl-VC-PABC-MMAE (5) (280 mg, 0.23 mmol) (Supporting Information Fig. S1).

Compounds **a**−**c** was made using regular solid-phase Fmoc peptide synthesis, where the final $CONH_2$ indicates C-terminal amide. The peptide was isolated from the resin by treating it with mixtures containing 95% trifluoroacetic acid (TFA), 1% β-mercaptoethanol, 2% water, and 2% triisopropylsilane (TIPS) for 4 h and filtered. This filtrate was concentrated and then precipitated by adding ice-cold ethyl ether. The precipitate is extracted by ice-cold ether/water (1:1), and then the water phase is dried using lyophilization to obtain crude peptide. The crude peptide was dissolved in water and purified by HPLC using 10%−40% acetonitrile in water and 0.1% TFA over 30 min at 6 mL/min flow rate. The purified product (compounds **a**−**c**) was dried using lyophilization.

Compounds **a**−**c** (100 mg) was added to a round-bottomed flask, followed by 50 mL of 20% DMSO aqueous solution and NH_4HCO_3 (40 mg, 0.5 mmol). The flask was opened and stirred at room temperature for 24 h. The solution was dried using lyophilization, and then the crude product was dissolved in water and purified by HPLC using 10%−40% acetonitrile in water and 0.1% TFA over 30 min at 6 mL/min flow rate. The purified product (T140-a, T140-b, and T140-c) was dried using lyophilization.

T140-a (19 mg, 0.009 mmol) dissolved in DMF (800 μL) was added to Alkynyl-VC-PABC-MMAE (11 mg, 0.009 mmol), and the aqueous solution (200 μL) of $CuSO_4 \cdot 5H_2O$ (2.3 mg, 0.009 mmol) and L-ascorbic acid sodium salt (VcNa) (3.6 mg, 0.018 mmol) was added with mixing. The mixture was stirred at room temperature for 12 h and then dried under vacuum. The crude product was dissolved in acetonitrile/water (1:1) and purified by HPLC using 10%−50% acetonitrile in water and 0.1% TFA over 40 min at 6 mL/min flow rate. The purified product was dried using lyophilization to obtain TM1 (20 mg, 0.006 mmol) (Supporting Information Fig. S2). HRMS (ESI): $C_{156}H_{242}N_{46}O_{32}S_2$ $[M+H]^{4+}$, calculated: 834.9614, found: 834.9620 (Supporting Information Fig. S3). Purity: >99.00% (Supporting Information Fig. S4).

T140-b (19 mg, 0.009 mmol) dissolved in DMF (800 μL) was added to Alkynyl-VC-PABC-MMAE (11 mg, 0.009 mmol), and the aqueous solution (200 μL) of $CuSO_4 \cdot 5H_2O$ (2.3 mg, 0.009 mmol) and VcNa (3.6 mg, 0.018 mmol) was added with mixing. The mixture was stirred at room temperature for 12 h and then dried under vacuum. The crude product was dissolved in acetonitrile/water (1:1) and purified by HPLC using 10%−50% acetonitrile in water and 0.1% TFA over 40 min at 6 mL/min flow rate. The purified product was dried using lyophilization to obtain TM2 (17 mg, 0.005 mmol) (Supporting Information Fig. S5). HRMS (ESI): $C_{156}H_{242}N_{46}O_{32}S_2$ $[M+H]^{4+}$, calculated: 834.9614, found: 834.9613 (Supporting Information Fig. S6). Purity: >99.00% (Supporting Information Fig. S7).

T140-c (24 mg, 0.009 mmol) dissolved in DMF (800 μL) was added to Alkynyl-VC-PABC-MMAE, and the aqueous solution (200 μL) of $CuSO_4 \cdot 5H_2O$ (2.3 mg, 0.009 mmol) and VcNa (3.6 mg, 0.018 mmol) was added with mixing. The mixture was stirred at room temperature for 12 h and then dried under vacuum. The crude product was dissolved in acetonitrile/water (1:1) and purified by HPLC using 10%−50% acetonitrile in water and 0.1% TFA over 40 min at 6 mL/min flow rate. The purified product was dried using lyophilization to obtain TFM (23 mg, 0.006 mmol) (Supporting Information Fig. S8). HRMS (ESI): $C_{181}H_{271}N_{55}O_{38}S_2$ $[M+H]^{3+}$, calculated: 972.7674, found: 972.7685 (Supporting Information Fig. S9). Purity: >99.00% (Supporting Information Fig. S10).

2.3. Synthesis of TF1, TF2 and TFF

Compounds **d**−**f** was made using regular solid-phase Fmoc peptide synthesis, where the final $CONH_2$ indicates C-terminal amide. It was isolated from the resin, purified by HPLC, and then engaged in disulfide cyclization as described for T140-a.

Compound **d** was cyclized to obtain TF1 (Supporting Information Fig. S11). HRMS (ESI): $C_{117}H_{163}N_{35}O_{24}S_3$ $[M+H]^{3+}$, calculated: 847.0664, found: 847.0633 (Supporting Information Fig. S12). Purity: 98.86% (Supporting Information Fig. S13).

Compound **e** was cyclized to obtain TF2 (Supporting Information Fig. S14). HRMS (ESI): $C_{111}H_{152}N_{34}O_{23}S_3$ $[M+H]^{3+}$, calculated: 809.3717, found: 809.3723 (Supporting Information Fig. S15). Purity: 97.61% (Supporting Information Fig. S16).

Compound **f** was cyclized to obtain TFF (Supporting Information Fig. S17). HRMS (ESI): $C_{142}H_{192}N_{44}O_{30}S_3$ $[M+H]^{4+}$, calculated: 773.3576, found: 773.3569 (Supporting Information Fig. S18). Purity: >99.00 (Supporting Information Fig. S19).

2.4. Cytotoxicity assay

The cells were placed in 96-well plates, exposed to the drug concentration range for 48 h, added with CCK-8, and incubated at 37 °C for 1−4 h. The absorbance (OD) was measured at 450 nm using Flex Station III Services (Thermo Fisher Scientific, Waltham, MA, USA). Then, the IC_{50} value was calculated using GraphPad Prism (GraphPad Software, San Diego, CA, USA).

2.5. Internalization experiment

To compare the differences between TF1 and TF2, MCF-7 seeded in a laser confocal dish was pretreated with TF1/TF2 (1 μmol/L) or DMSO (1%, *v*/*v*) at 37 °C for 4 h and then incubated with Lyso-Tracker Red (C1046, Beyotime, Shanghai, China) at 37 °C for 1 h. Subsequently, cells were washed with PBS three times and fixed in 4% paraformaldehyde for 10 min at room temperature. Cells were washed with PBS three times, incubated with DAPI (C0065, Solarbio, Beijing, China) and imaged by confocal microscope (Zeiss, Oberkochen, Germany). For the comparison between TF2 and TFF, the pretreatment concentration of TF2/TFF was 1 μmol/L, and the competitive concentration of T140 and FA was 10 μmol/L.

2.6. Cathepsin B-mediated MMAE release of TM1 and TM2

The TM1 and TM2 stock solution (10 mmol/L) was diluted into 0.1 mmol/L solution using 100 mmol/L L-lys (pH = 6). Next, cathepsin B (Sigma, St. Louis, MO, USA; cat. no. C8571, ≥1500 units/mg protein, ∼15.7 mmol/L) was added into solution (∼9 μg/mL), and the reaction mixture was incubated at 37 °C. Aliquots were evaluated at 0, 1, 6, 18, 24, 30, 42, and 48 h using LC−MS/MS. Concentrations of released MMAE (nmol/L) were quantified using the standard curve method.

2.7. Blood cell counts and bone marrow smear staining

Six BALB/c mice were divided evenly into two groups, including the control group and the experiment group. Mice in the experimental group were intraperitoneally injected with TFM (1 mg/kg/day) for three consecutive days, and the control group mice were injected with an equal volume of saline. On Day 4, the blood and marrow were taken for blood cell counts and bone marrow smear staining.

2.8. Immunoblotting

Cells were harvested and lysed in RIPA buffer (Solarbio, Beijing, China) with protease and phosphatase inhibitors, and the concentration of whole protein was calculated using the BCA kit (Thermo Fisher Scientific, Waltham, MA, USA). The protein was transferred to polyvinylidene fluoride after 10% SDS-PAGE separation and incubated with indicated primary antibodies CXCR4 (Affinity, #AF5279, dilution 1:1000, Melbourne, Australia), FOLR1 (Affinity, #DF4058, dilution 1:500), caspase-3 (Abcam, #ab32351, dilution 1:5000, Cambridge, UK), cleaved caspase-3 (CST, #9661, dilution 1:1000, Boston, MA, USA), PARP (CST, #9532, dilution 1:1000), HMGB1 (Affinity, #AF7020, dilution 1:1000) and β-actin (Affinity, #AF7018, dilution 1: 5000). After that, the polyvinylidene fluoride was incubated with the appropriate secondary antibodies (Beyotime, A0208, dilution 1:2000, Shanghai, China). Blots were developed by ECL (NCM, Suzhou, China).

2.9. Cell apoptosis

Cells were treated with TFM for 24 h at 37 °C, and then cells were collected, washed with PBS, dispersed in staining buffer and incubated with Annexin V/PI stain kit (Beyotime, Shanghai, China). After incubation in the dark for 15 min, cells were detected by a Flow cytometer (NovoCyte Quanteon, Agilent, San Jose, CA, USA).

2.10. Cell cycle

After treatment with TFM for 24 h at 37 °C, cells were collected, washed with PBS, and fixed in 70% ethanol overnight at 4 °C. Then cells were washed with PBS, stained with propidium iodide dye (KeyGEN Biotech, Nanjing, China), and then detected by a Flow cytometer (NovoCyte Quanteon, Agilent, San Jose, CA, USA).

2.11. Human xenograft tumor models and treatments

Female athymic BALB/c nude mice aged 6 weeks were purchased from Huachuang Sino (Taizhou, China), keeping in the SPF condition. For the MCF-7 xenograft model, we subcutaneously injected 5×10^6 MCF-7 cells suspended in 100 μL PBS into the right flank of nude mice. PDCs (TM1/TM2/TFM) were administered at a dose of 0.5 mg/kg every 2 days when the tumor volume was about 80 mm^3 with the normal saline as negative control. The tumor volumes and body weights were recorded every 2 days during treatment.

For the MDA-MB-231 xenograft model, a total of 5×10^6 MDA-MB-231 cells were suspended in a 100 μL mixture of Matrigel matrix and PBS (1:1) and injected subcutaneously into the right flank of nude mice. We randomly arranged BALB/c nude mice with a tumor volume of at least 80 mm^3 into five groups. The mice were intraperitoneally injected with three doses of TFM: low-dose (0.1 mg/kg), medium-dose (0.5 mg/kg), and high-dose (1 mg/kg) respectively. Paclitaxel (PTX, 4 mg/kg) was used as a positive control, and the negative control group mice were injected with PBS. Each group of mice was administered every three days, and tumor volume and body weight were recorded. The tumors were caught out and weighed after the mice were euthanized. All experimental procedures were executed according to the protocols approved by Lanzhou University Animal Care and Use Committee (Lzujcyxy20230321).

2.12. Histological analysis

Tumor sections were dyed with the CXCR4 antibody (diluted at 1:100) at 4 °C overnight. Then, the sections were washed three times with PBS and incubated with HRP-conjugated secondary antibody (PV-9001, ZSGB-BIO, Beijing, China) for 30 min. Finally, the sections were stained by DAB chromogenic reagent (ZLI-9017, ZSGB-BIO, Beijing, China) and observed under a microscope. For histomorphometric analysis, sectioned organs were then stained with hematoxylin-eosin. Then, these sections were photographed using a NIS-element imaging system (Nikon, Tokyo, Japan).

2.13. Serum stability test

TFM was dissolved in PBS and diluted with mouse serum to the concentration of 0.5 mmol/L and incubated in a water bath at 37 °C for 0, 1, 2, 4, 6, 12, and 24 h, respectively. Then, an equal volume of ice acetonitrile was mixed with the incubator and incubated at 60 °C for 15 min to inactivate the serum. The mixture was centrifuged, and the supernatant was used for HPLC detection.

2.14. Hemolysis test

BALB/c mice blood was collected in centrifuge tubes added the prepared heparin sodium in advance. In a 96-well plate, 100 μL PBS solution of TFM (512, 256, 128, 64, 32, 16 and 4 μg/mL) and 100 μL plasma were added to each well. The positive and negative control was added with 2% Triton and PBS respectively. The absorbance of plate was detected at 490 nm.

2.15. Transwell assay

4T1 cells were seeded into 24-well plates (Transwell insert top chamber) at a concentration of 5×10^4 cells per well. 200 μL 1640 medium containing 2% FBS was added to the top chamber, and 600 μL 1640 medium containing 2% FBS was added to the bottom chamber. After treatment with different concentrations of TFM for 24 h, the top chambers were cleaned to remove non-migrated cells, and the inserts were stained with Crystal violet

(Solarbio, Beijing, China). Photos were taken under an inverted microscope, and data were analyzed by GraphPad Prism.

2.16. Animal lung metastatic model establishment

Female BALB/c mice aged 6 weeks were purchased from Huachuang Sino (Taizhou, China) and fed at 22 °C with a diurnal cycle. A total of 8×10^5 4T1-luci cells suspended in 100 μL PBS were injected gently *via* the tail vein to each mouse. After 2 days, T140 and TFM were i.v. injected every 2 days, and the mice were monitored by VISQUE *in vivo* Smart-LF (Vieworks, Seoul, Korea) on Days 4, 8, 12, and 16. After the mice were euthanized, the lungs of mice were taken out and preserved with 4% paraformaldehyde for HE staining.

2.17. Combined therapy for 4T1 transplanted tumor

Female BALB/c mice aged 6 weeks were purchased from Huachuang Sino (Taizhou, China) and fed at 22 °C with a diurnal cycle. A total of 1×10^6 4T1 cells suspended in 100 μL PBS were injected subcutaneously into the right flank of BALB/c mice. Five days after implantation, mice were treated with either TFM (0.5 mg/kg), IR, and IR + TFM (0.5 mg/kg) as indicated in figure legends, with the normal saline as negative control. Tumor targets were delineated and given 10 Gy for each mouse using a Small Animal Image-guided Radiation Therapy System (X-RAD smart, PRECISION X-RAY INC, Glendale, CA, USA) on Days 0 and 10, respectively. The tumors were caught out and weighed after the mice were euthanized.

2.18. Flow cytometry analysis

4T1 Tumors were isolated with fatty tissue and mucous membranes removed, and then tumors were minced and placed in the centrifuge tube. Tumor fragments were detached with trypsin for 5 min and subsequently mixed with the same volume of FBS-free DMEM media. The preceding steps were repeated five times, and the collected mixed solution was centrifuged and suspended in PBS to obtain single-cell suspension. The viable cells were determined by Trypan blue staining. Cells were washed and stained for surface markers for 30 min at 4 °C. Antibodies (clone in parenthesis) were purchased from BioLegend (San Diego, CA, USA) and included FITC anti-mouse CD3 Antibody (17A2), PerCP anti-mouse CD4 Antibody (RM4-5), APC anti-mouse CD8a Antibody (53-6.7), Brilliant Violet 421™ anti-mouse CD45 Antibody (30-F11), PE/Cyanine7 anti-human/mouse Granzyme B Recombinant Antibody (QA16A02), PE/Cyanine7 anti-mouse CD25 Antibody (3C7), PE anti-mouse Ly-6G/Ly-6C (Gr-1) Antibody (RB6-8C5), APC anti-mouse/human CD11b Antibody (M1/70). All flow cytometry data acquisition was done using a Flow cytometer (NovoCyte Quanteon, Agilent, San Jose, CA, USA) and analyzed using FlowJo software (BDBiosciences, Franklin Lakes, NJ, USA).

2.19. In vitro induction of immunogenic cell death

For the investigation of the CRT exposure on the cell surface, 4T1 cells were seeded onto the coverslips and then treated with TFM for 48 h. After treatments for 48 h, cells cells were fixed with 4% paraformaldehyde and blocked with 1% BSA. Afterward, cells were incubated with anti-CRT antibody (CST, #12238, dilution 1:500) at 4 °C overnight and then stained with Alexa Fluor 555-conjugated secondary antibody (Abclonal, #AS057, dilution 1:250) at room temperature for 1 h. Finally, the nuclei were stained with DAPI, and cells were observed by a confocal microscope (Zeiss, Oberkochen, Germany).

To quantitatively detect the amount of released ATP, 4T1 cells were incubated with TFM for 48 h. The medium was collected and centrifugated to remove cell debris. The supernatant was measured using the protocol of a luciferase-based ATP assay kit (S0026, Beyotime, Shanghai, China).

For the detection of the intracellular and extracellular HMGB1 protein, 4T1 cells were treated with TFM for 48 h. Cell culture supernatant and cells were collected for immunoblotting. β-Actin was used as the control protein.

2.20. In vivo toxicity analysis

The mouse plasma samples were centrifuged to obtain supernatant. We assessed the liver function (ALT, AST, ALB, ALP, and GGT) and renal function (BUN, CR, and UA) using an automatic biochemical analyzer (Chemray 800, Rayto, Shenzhen, China).

2.21. B16F10 transplanted tumor model and treatment

Female C57BL/6 mice aged 6 weeks were purchased from Huachuang Sino (Taizhou, China) and fed at 22 °C with a diurnal cycle. A total of 5×10^5 B16F10 cells suspended in 100 μL PBS were injected subcutaneously into the right flank of C57BL/6 mice. 0.5 mg/kg TFM was administered every 2 days when the tumor volume was about 50 mm^3 with the normal saline as negative control. The tumors were caught out and weighed after the mice were euthanized. All experimental procedures were executed according to the protocols approved by Lanzhou University Animal Care and Use Committee.

2.22. Synthesis of TFD and radionuclide labeling

Compound **g** was made using regular solid phase Fmoc peptide synthesis, where the final $CONH_2$ indicates C-terminal amide. The Compound **g** was isolated from the resin, purified by HPLC and then engaged in disulfide cyclization as described for T140-a.

Compound **g** was cyclized to obtain TFD (Supporting Information Fig. S20). HRMS (ESI): $C_{131}H_{197}N_{47}O_{30}S_2$ $[M+H]^{4+}$, calculated: 744.3773, found: 744.3756 (Supporting Information Fig. S21). Purity: >99.00% (Supporting Information Fig. S22). 20 μg TFD was mixed with $^{64}CuCl_2$ (500−1000 μCi, 0.1 mol/L NaOAc, pH = 4.1), and the reaction mixture was heated to 80 °C for 10 min.

2.23. Small-animal PET study

PET scans were performed using a small-animal PET/CT (MadicLAB PSA094, Shandong Madic Technology, China). The labeled [^{64}Cu]TFD was diluted with normal saline and was injected 200 μCi into tumor-bearing mice *via* the tail vein, and PET/CT imaging was performed at different times.

For block assay, before injecting MCF-7 tumor-bearing mice with [^{68}Ga]TFD (300 μCi/mouse), we injected TFD (50 μg/mouse) 30 min in advance, and static PET images were acquired 1 h postinjection.

Images were reconstructed by a three-dimensional ordered subsets expectation maximum (3D OSEM) algorithm without correction for attenuation or scatter. The CT data from the PET/

CT examination were reconstructed in the transverse plane as 0.1 mm thick sections. The following parameters were used for imaging: 80 kV, 70 mAs. The radioactivity was decay-corrected for the injection time and expressed as the percent of the total injection dose/per cubic centimeter (%ID/cc).

2.24. Statistical analysis

Quantitative data are presented as the mean ± standard eror of mean (SEM) of at least three independent experiments. The statistical analysis was conducted using GraphPad Prism 8.0.1 software based on two-tailed, unpaired Student's *t*-test and One-way ANOVA. Differences were considered significant at *P*-values of <0.05, 0.01, and 0.001, respectively.

3. Results

3.1. Synthesis and antitumor activity evaluation of PDCs that target CXCR4

As CXCR4 is highly expressed in breast cancer, including the cell lines MCF-7, MDA-MB-231, and 4T1 (Supporting Information Figs. S23 and S24), we chose T140, a CXCR4 antagonist peptide containing fourteen amino acids, as a targeting ligand for constructing PDCs (Fig. 1A and Supporting Information Fig. S25). We also included in our design the Val-Cit-PABC linker (Fig. S1), which is self-immolative in the presence of cathepsin B and has been validated in ADCs for clinical cancer treatment[41], as well as MMAE, a tubulin polymerization inhibitor that is widely used as the payload in ADCs[42]. To reduce the toxicity of MMAE to normal tissues and enhance the tumor-targeting capability, we employed two reactive sites in T140 for coupling to MMAE: the N-terminal arginine and the D-lysine in the middle of the peptide chain[43]. Consequently, TM1 and TM2 were designed and synthesized (Figs. S2 and S5). To compare the effect of the two reactive sites on PDC function, we performed cell counting kit-8 (CCK8) (New Cell & Molecular Biotech Co., Ltd., Suzhou, China) assays of the antiproliferative activity in MCF-7 cells. The IC_{50} of TM1 and TM2 were 4.05 ± 2.32 and 3.98 ± 1.68 μmol/L, respectively (Fig. 1B), while the IC_{50} of T140 (without conjugated MMAE) was undetectable within the same dilution concentration range (Supporting Information Table S1).

To compare the effect of the different reactive sites on internalization, we replaced MMAE with FITC to produce TF1 and TF2 (Figs. S11 and S14). At a concentration of 1 μmol/L, a more pronounced green fluorescence was observed in MCF-7 cells cultivated with TF2 as compared to TF1 (Fig. 1C). In addition, TF1 and TF2 colocalized to lysosomes regardless of the intensity of the green fluorescence. Given that cathepsin B is highly expressed in lysosomes, the colocalization of TF1 and TF2 within the lysosomes suggests that the binding of T140 to CXCR4 might facilitate entry into the lysosome, degradation of the VC-PABC linker by cathepsin B, and MMAE release to confer the cytotoxicity of TM1 and TM2. These results also suggest that D-lysine is a more desirable position for introducing functional groups, which may be because the introduction of MMAE at the N-terminal arginine impedes the binding of T140 and CXCR4 *via* essential N-terminal amino acid residues[44]. In order to study the effect of different reactive sites on enzymatic hydrolysis, we carried out the cathepsin B cleavage experiment. After cathepsin B treatment, the MMAE generation rate of TM1 was significantly faster than TM2 (Supporting Information Fig. S26). The above results indicate that although the internalization level of TF1 is weaker than that of TF2, TM1 can lysate and release MMAE faster than TM2 in the presence of cathepsin B.

To probe the *in vivo* effect of PDCs, we established xenograft models using MCF-7 cells in BALB/c nude mice. Tumor growth kinetic studies and tumor weight data demonstrate the effectiveness of TM1 and TM2 in inhibiting the growth of MCF-7 xenografts. Consistent with the colocalization results, the average tumor weight of the TM2 treatment group was significantly smaller than that of the TM1 treatment group (Fig. 1D and E). No significant decrease in body weight was observed, suggesting that the PDCs have good tolerance (Fig. 1F).

3.2. Synthesis and antitumor activity evaluation of PDCs that target both CXCR4 and FOLR1

To enhance the targeting and internalization efficiency of the CXCR4-targeting PDC, we added FA to TF2 and TM2 for dual targeting and synthesized TFM and TFF (Fig. 2A; Figs. S8 and S17). In CCK8 assays, TFM showed better anti-proliferative activity than TM2, with an IC_{50} of 2.01 ± 0.39 μmol/L against MCF-7 cells (Fig. 2B, Table S1). To verify that the dual ligand strategy increased the internalization efficiency, we performed fluorescence and flow cytometry experiments. Cells treated with TFF displayed notable green fluorescence that was colocalized in lysosomes under confocal microscopy, while cells treated with TF2 only displayed faint green fluorescence. Furthermore, the addition of free T140 or FA to the cell culture blocked the internalization of the PDCs, thus confirming the role of CXCR4/FOLR1 (Fig. 2C). In addition to MCF-7 cells, we also obtained the same results in MDA-MB-231 cells (Supporting Information Fig. S27A and S27B). As additional verification, flow cytometry quantitatively yielded similar results (Fig. 2D) and demonstrated that the enhancement of fluorescence intensity was dose-dependent (Fig. S27C and S27D). Moreover, in MCF-10A cells, which have low expression of CXCR4 and FOLR1, we observed minimal green fluorescence under confocal microscopy and small changes of fluorescence signal by flow cytometry after culture with TF2/TFF (Fig. S27E and S27F). These results suggest that the PDCs enter into cells *via* the lysosomal pathway mediated by CXCR4 and FOLR1; however, dual-targeting PDCs have higher internalization efficiency and stronger anti-proliferative activity than PDCs targeting CXCR4 alone.

3.3. Apoptosis and cell cycle arrest of tumor cells induced by TFM

To verify that TFM recapitulates the mechanism as MMAE in inhibiting the tumor cell growth, we performed apoptosis analysis using MDA-MB-231 TNBC cells, which have higher expression of CXCR4 and FOLR1 than in MCF-7 cells (Fig. S24). Double staining with annexin V-FITC/propidium iodide demonstrated that the percentage of total apoptotic cells surged from 4.08% in the control group to 23.40% in the 1000 nmol/L TFM group (Fig. 3A and B). Consistently, immunoblot assays revealed enhanced protein levels of the apoptosis markers cleaved caspase-3 and cleaved-PARP with increasing TFM concentration (Fig. 3C and D). Cell cycle analysis further demonstrated that the proportion of cells in the G2/M phase was significantly increased in the 500 nmol/L TFM group (Fig. 3E and F). Taken together, our data

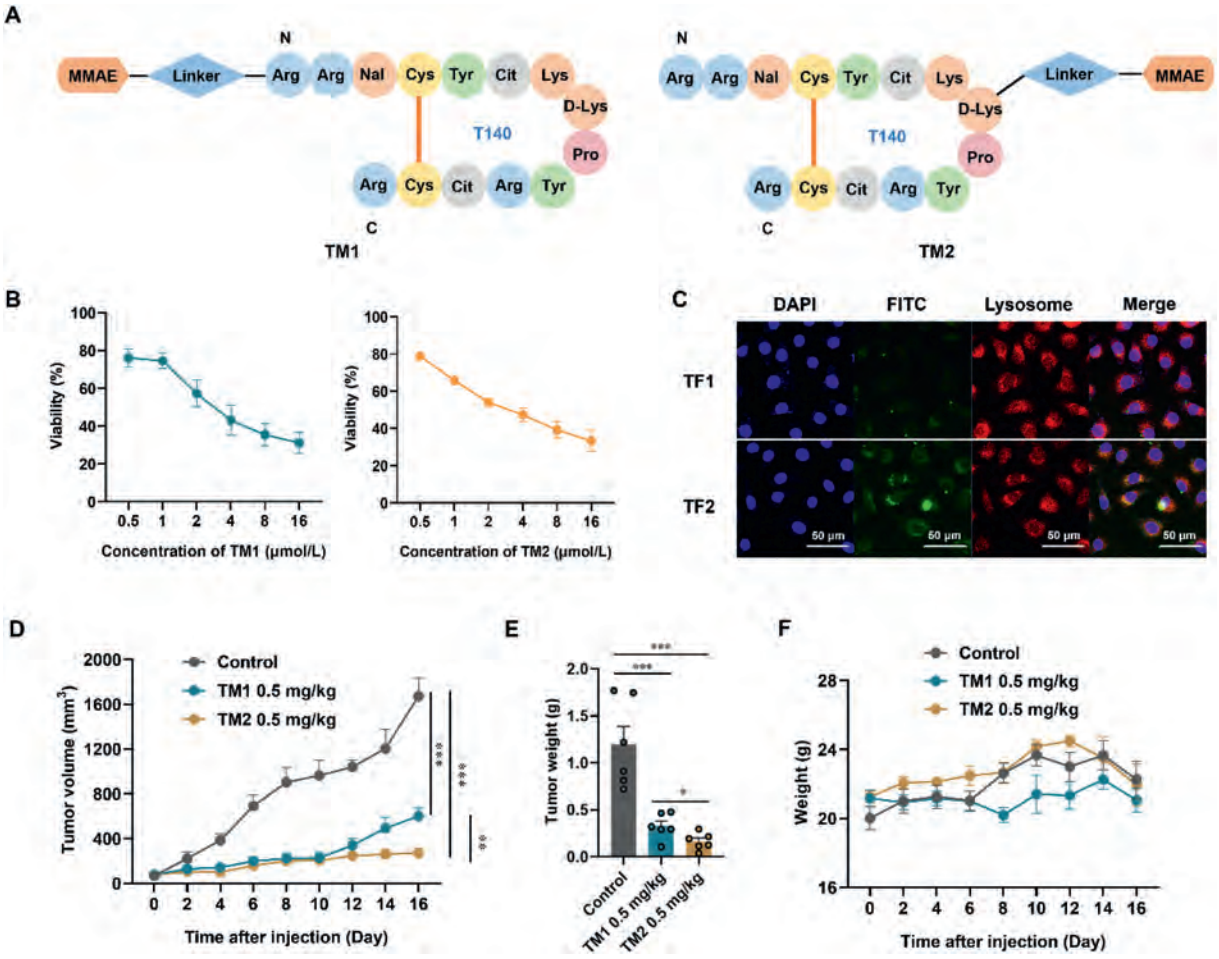

Figure 1 PDCs targeting CXCR4 have effective antitumor activity. (A) Structural representation of TM1 and TM2. (B) CCK8 assay of the cellular activity of TM1 and TM2 against MCF-7. (C) Confocal fluorescence images show that TF1 and TF2 (10 μmol/L, 4 h) can enter MCF-7 cells through CXCR4-mediated internalization. Scale bar = 50 μm. (D) Tumor growth kinetics (mean ± SEM, $n = 6$) of MCF-7 tumor-bearing BALB/c nude mice treated with saline (control), TM1 or TM2. (E) Tumor weight (mean ± SEM, $n = 6$) of MCF-7 tumor-bearing BALB/c nude mice treated with saline, TM1 or TM2. (F) The weight of MCF-7 tumor-bearing BALB/c nude mice treated by saline, TM1 and TM2 (mean ± SEM, $n = 6$). Data in (D) and (E) were analyzed by two-tailed unpaired Student's *t*-test, $^*P < 0.05$, $^{**}P < 0.01$, $^{***}P < 0.001$.

confirm that TFM can induce apoptosis and block cell cycle progression.

3.4. The inhibition of cancer progression in TNBC xenograft models by TFM and PET imaging in tumors of TFD

Given the effective internalization and inhibition of breast cancer cells by TFM, we speculated that it may have therapeutic activity in a mouse model. Before assessing the antitumor activity of TFM, we evaluated its serum half-life, which was 16.85 h, indicating satisfactory stability (Supporting Information Fig. S28A and S28B). We also verified that TFM has no measurable hemolytic toxicity (Fig. S28C and S28D). Furthermore, we investigated the safety of TFM in the blood and bone marrow of BALB/c mice, and the results showed that TFM did not cause changes in blood cells and bone marrow (Fig. S28E−S28G). Next, we evaluated the antitumor activity of TFM compared with TM2 in an MCF-7 xenograft model. The results showed that the activity of TFM was superior to that of TM2 in inhibiting the progression in MCF-7 tumors (Fig. 4A and B), with no significant decrease in body weight (Fig. 4C). The tumor growth inhibition rate (TGI) of TFM was 85%, while the TGI of TM2 was 73%.

Since the breakthrough therapeutic effect of ^{177}Lu-DOTATATE and ^{177}Lu-PSMA-617, the field of innovative nuclear drugs has received extensive attention, and the integration of diagnosis, treatment, and PRCs has become a prominent research focus. Therefore, we designed and synthesized a double-targeted PET tracer ([^{64}Cu]TFD) by adding DOTA instead of the MMAE in TFM *via* a lysine linker (Fig. S20). In MCF-7 tumor-bearing mice, we observed [^{64}Cu]TFD uptake in tumors at 1−8 h after injection, with a slight decline at 20 h, potentially explained by ^{64}Cu decay ($t_{1/2} = 12.7$ h) (Fig. 4D and Supporting Information Fig. S29A). Given this, we further labeled TFD with ^{68}Ga and studied its imaging performance. PET imaging showed a notable accumulation of [^{68}Ga]TFD in the tumor during 1 h. In contrast, a significant reduction in radioactivity uptake was observed in the MCF-7 tumor when they received a blocking dose of TFD (Fig. 4E and Fig. S29B), which confirmed the *in vivo* binding specificity of [^{68}Ga]TFD toward CXCR4 and FOLR1. These results verify the efficient uptake of [^{64}Cu]TFD or [^{68}Ga]TFD in MCF-7-derived

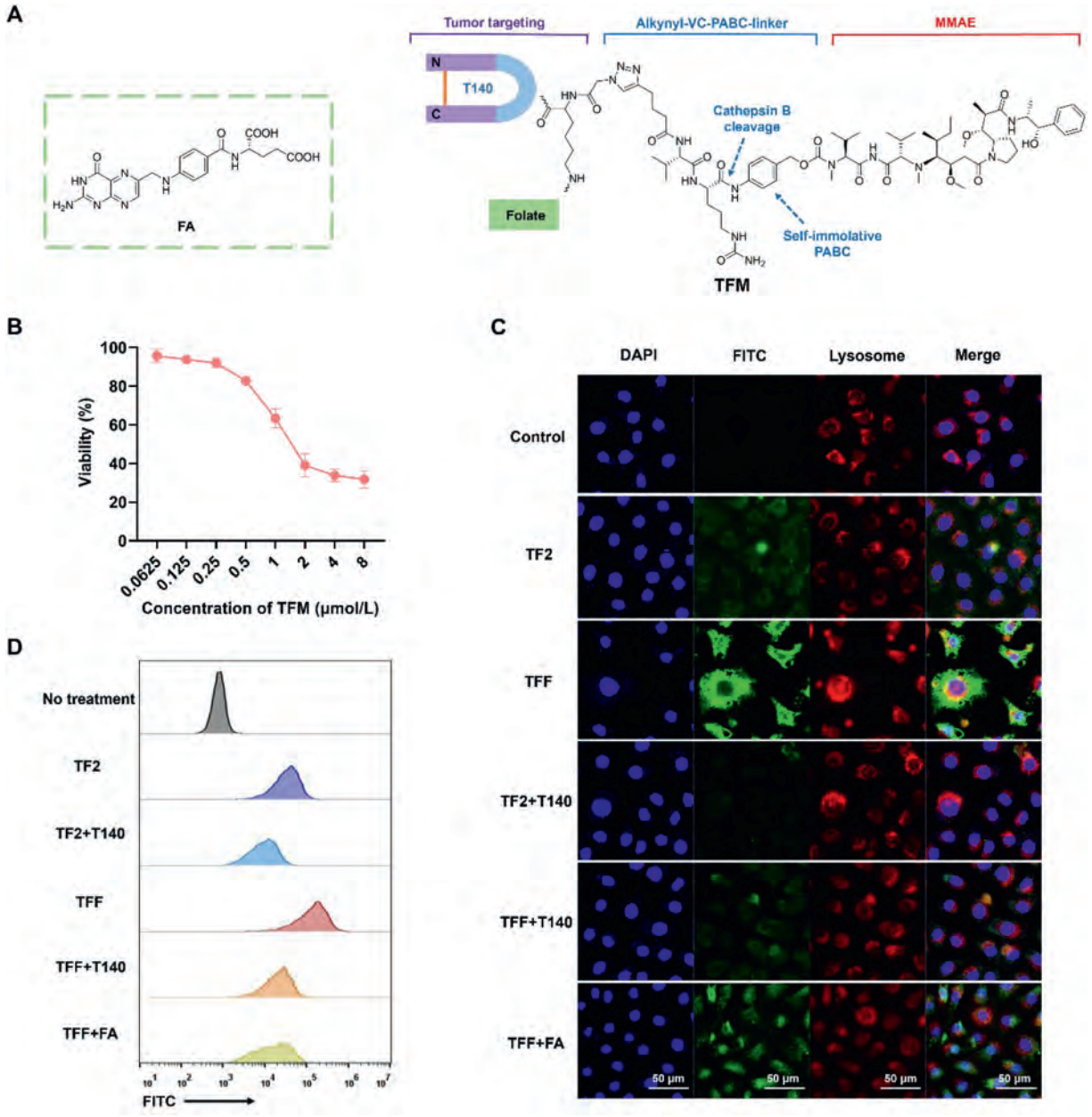

Figure 2 The dual targeting strategy enhances the internalization of PDCs. (A) Structural representation of TFM and schema of T140 and FA conjugated to MMAE using the Alkynyl-VC-PABC linker. (B) CCK8 assay of the cellular activity of TFM against MCF-7 ($n = 3$). (C) Confocal fluorescence images showing the internalization of TF2 and TFF (1 μmol/L, 4 h) in MCF-7 cells. Where indicated, the cells were cultured with T140 or FA (10 μmol/L) for 1 h to block PDC entry into cells. Scale bar = 50 μm. (D) Flow cytometry analysis of MCF-7 cells treated by TF2 and TFF with or without the competition.

tumors in mice and suggest that TFD may provide a useful tool for tumor imaging. In addition, to further validate the uptake of [^{64}Cu]TFD in TNBC tumors, we investigated the PET imaging of [^{64}Cu]TFD on MDA-MB-231 tumor-bearing mice and 4T1 tumor-bearing mice. Similar to the results in MCF-7 tumor-bearing mice, [^{64}Cu]TFD was also significantly taken up in two types of TNBC tumors (Fig. S29C−S29F), implying the therapeutic effect of TFM on TNBC xenograft.

For additional confirmation of the antitumor effects of TFM, we investigated its efficacy at three different doses in the MDA-MB-231 xenograft model. As free MMAE is too toxic to be injected intravenously *in vivo* [45], we selected paclitaxel (PTX) as a positive control drug. Our data demonstrated that all TFM administration groups had potent therapeutic effects that were comparable to that of PTX (Fig. 4F and G), without a significant decrease in mice body weight (Fig. 4H). Notably, these results show complete tumor regression (CR) in four of the six mice in the high-dose group on Day 24 and approximately two-fold lower tumor weight in the medium-dose group than in the PTX treatment group. Tunel staining and Ki67 staining further demonstrated that there was a large proportion of apoptotic cells and a small proportion of proliferative cells in the PTX-treated group and medium-dose treatment group (Fig. 4I), which is consistent with our *in vitro* data. Moreover, immunohistochemical staining of

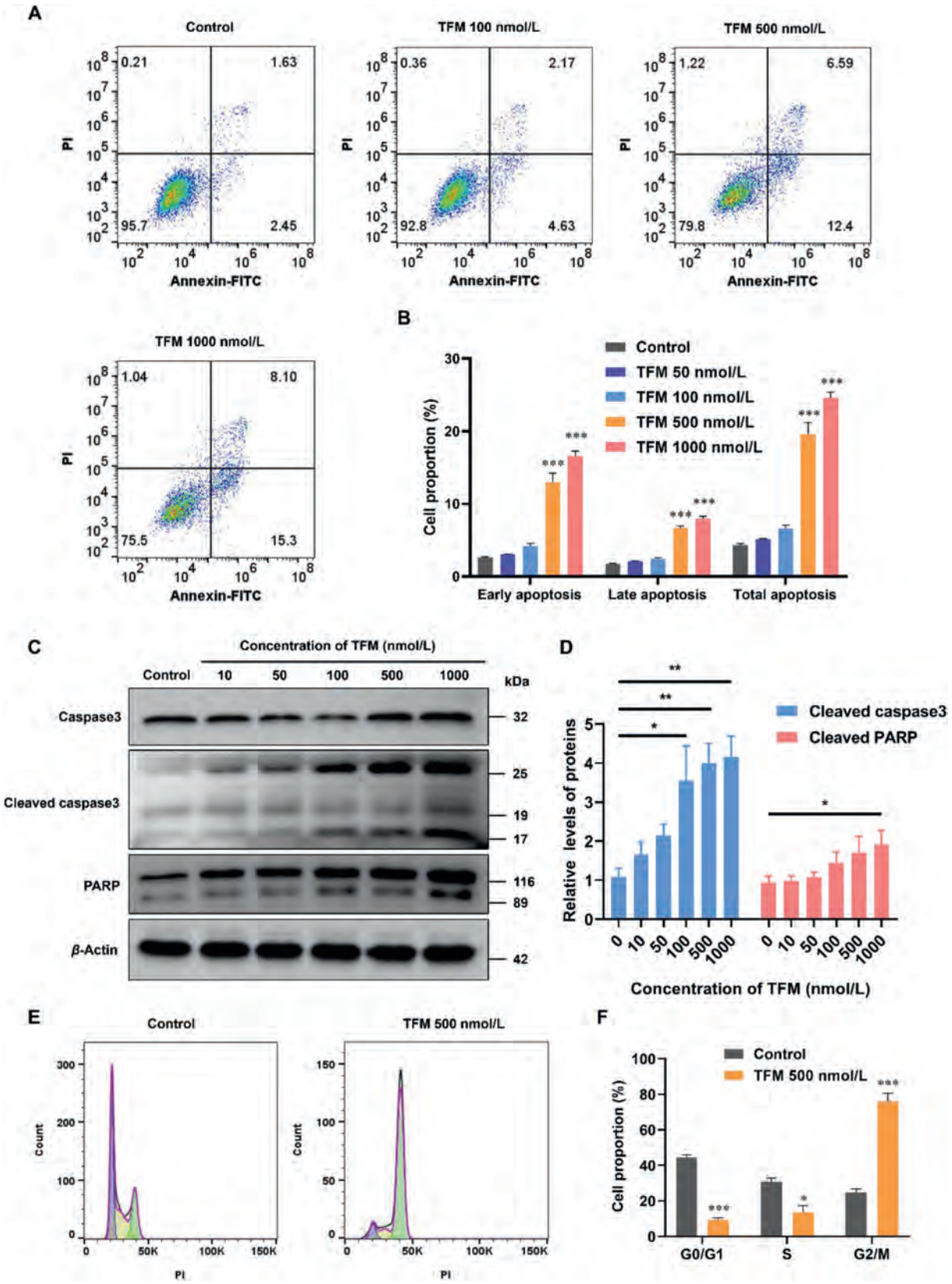

Figure 3 TFM induces MDA-MB-231 cell apoptosis and cell cycle arrest. (A) Flow cytometry analysis showing the apoptosis induced by treating MDA-MB-231 cells with different concentrations of TFM for 24 h. (B) The proportion of early and late apoptotic cells induced by different concentrations of TFM (mean ± SEM, $n = 3$). (C) Changes in apoptosis pathway-related protein levels after exposure to TFM. (D) The semi-quantitative analysis data of apoptosis pathway-related protein levels. (E) The proportion of cells at different stages of cell division (mean ± SEM, $n = 3$). (F) Flow cytometry analysis showing cell cycle arrest in the G2/M phase caused by TFM. Data in (B) were analyzed by one-way ANOVA. Data in (D) and (F) were analyzed by the one-tailed unpaired Student's *t*-test, $^{*}P < 0.05$, $^{**}P < 0.01$, $^{***}P < 0.001$.

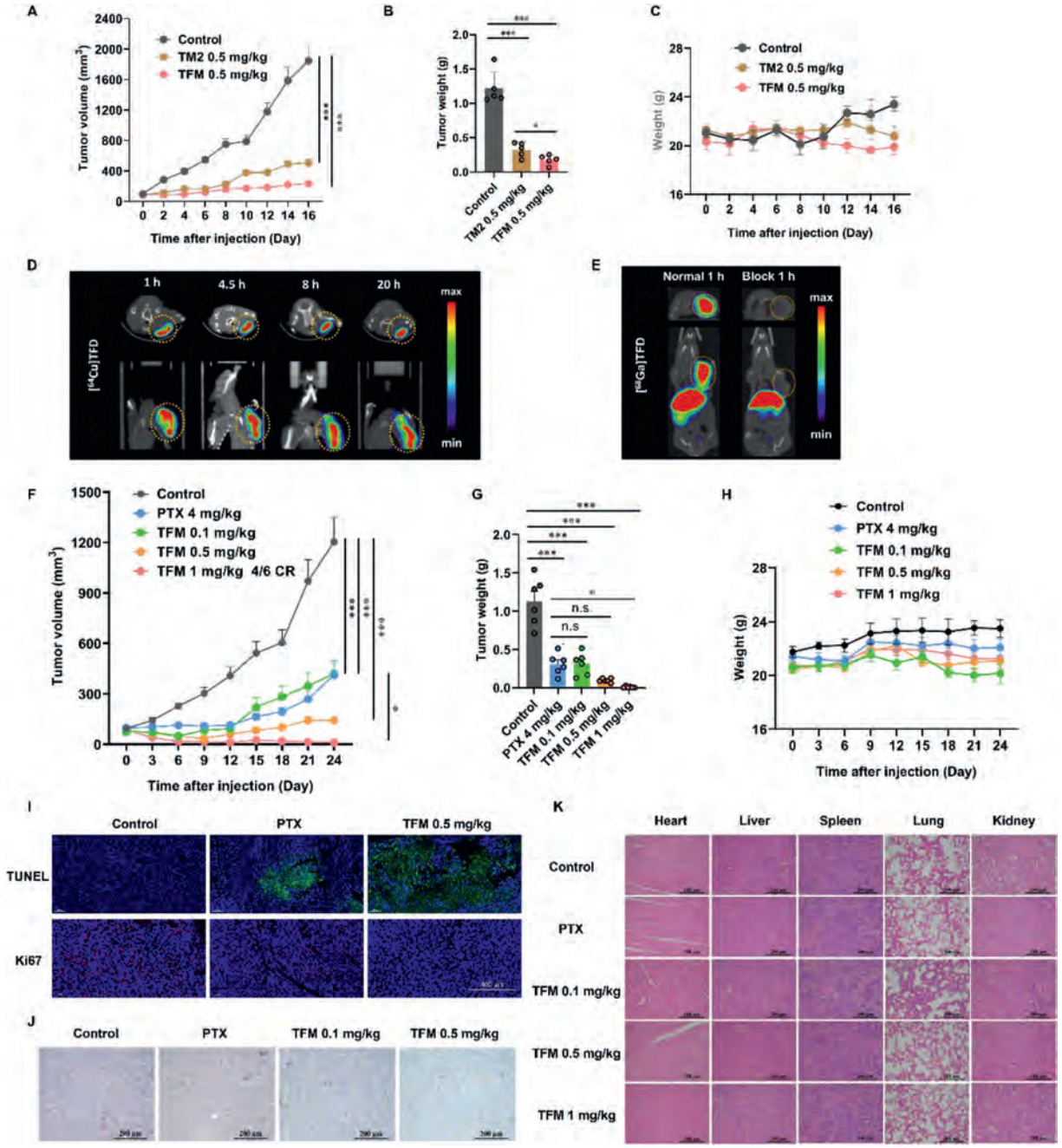

Figure 4 TFM is effective against TNBC xenograft models. (A to C) Tumor growth kinetics (mean ± SEM, $n = 5$) (A), tumor weight (mean ± SEM, $n = 5$) (B), and mouse body weight changes (mean ± SEM, $n = 5$) (C) of MCF-7 tumor-bearing BALB/c nude mice treated with saline, TM2 and TFM. (D) Micro-PET images of MCF-7-bearing mice after injection of [^{64}Cu]TFD. The pictures above show the longitudinal section, and the pictures below show the transverse section. (E) Micro-PET images of MCF-7-bearing mice after injection of [^{68}Ga]TFD. The pictures above show the longitudinal section, and the pictures below show the transverse section. (F to H) Tumor growth kinetics (mean ± SEM, $n = 6$) (F), tumor weight (mean ± SEM, $n = 6$) (G), and mouse body weight changes (mean ± SEM, $n = 6$) (H) in MDA-MB-231 tumor-bearing BALB/c nude mice treated with saline, pacitaxel (PTX), or low, medium, and high doses of TFM. (I) Tunel and Ki67 staining of MDA-MB-231 tumors from mice treated with saline, PTX, or 0.5 mg/kg TFM. Scale bar = 400 μm. (J) Representative immunohistochemical staining of MDA-MB-231 tumors corresponding to different drug treatment groups to evaluate the levels of CXCR4 expression. Scale bar = 200 μm. (K) H&E staining of major organs from MDA-MB-231 tumor-bearing mice. Scale bar = 200 μm. Data in (A), (B), (F), and (G) were analyzed by one-way ANOVA, $^{*}P < 0.05$, $^{**}P < 0.01$, $^{***}P < 0.001$. n.s., not significant.

tumor tissues validated that the proportion of CXCR4-positive cells was significantly lower in the TFM-treated group compared with the control group, whereas PTX had little effect on the number of CXCR4-positive cells (Fig. 4J). Finally, we did not observe any significant morphological differences in vital organs, including the liver, lung, heart, kidney, and spleen, by hematoxylin

and eosin (H&E) staining of the administration and control groups (Fig. 4K). Collectively, these results indicate that TFM is highly effective in suppressing tumor growth in MCF-7 and MDA-MB-231 xenograft models.

3.5. *The inhibition of the TNBC cells metastasis by TFM*

As CXCR4 is inextricably linked to tumor metastasis, we sought to investigate the effect of TFM on the metastasis of TNBC cells to the lung. For this purpose, we selected 4T1, a highly invasive murine-derived TNBC cell line that expresses both CXCR4 and FOLR1 (Fig. S24). First, we assessed the effect of TFM and free T140 peptide on the invasion ability of 4T1 cells using Transwell assays. T140 and TFM each displayed significant anti-metastasis activity, thus verifying that the blockade of CXCR4 inhibits 4T1 cell migration (Fig. 5A and B). Next, we evaluated the *in vivo* effects of T140 and TFM on the homing and lung-specific colonization of circulating tumor cells. T140 failed to prevent the metastasis and growth of 4T1 cells in the lungs, as the luminescence intensity reached 3.89×10^6 p/s, with no significant difference compared with the control group (4.05×10^6 p/s). However, the TFM-treated group showed weaker luminescence signals (1.25×10^6 p/s), suggesting that TFM inhibits the metastasis and growth of 4T1 cells in the lung (Fig. 5C and D). For additional confirmation, we dissected the lungs on Day 17, which we stained with HE. Significant metastatic nodules were visible on the lungs of the control and T140-treated groups, while the nodules in the TFM group were much smaller (Fig. 5E). These results indicate that TFM impedes the *in vivo* migration of cancer cells and has the ability to significantly suppress tumor metastasis to the lung.

3.6. *The synergistic inhibition of tumor growth by the combination of TFM and irradiation*

Evidence has shown that MMAE can radiosensitize tumor cells, resulting in increased amounts of DNA double-strand breaks in irradiated cells[46]. To interrogate whether TFM has the same radiosensitizing effect, we combined TFM and irradiation (IR). 4T1 tumor-bearing mice were treated with localized 10 Gy IR on Days 0 and 10, and then they were treated with or without TFM every 2 days until Day 18 (Fig. 6A). The results demonstrate that TFM or IR alone slowed tumor progression, whereas the combination treatment effectively controlled tumor growth (Fig. 6B and Supporting Information Fig. S30). The TGI of the TFM and IR

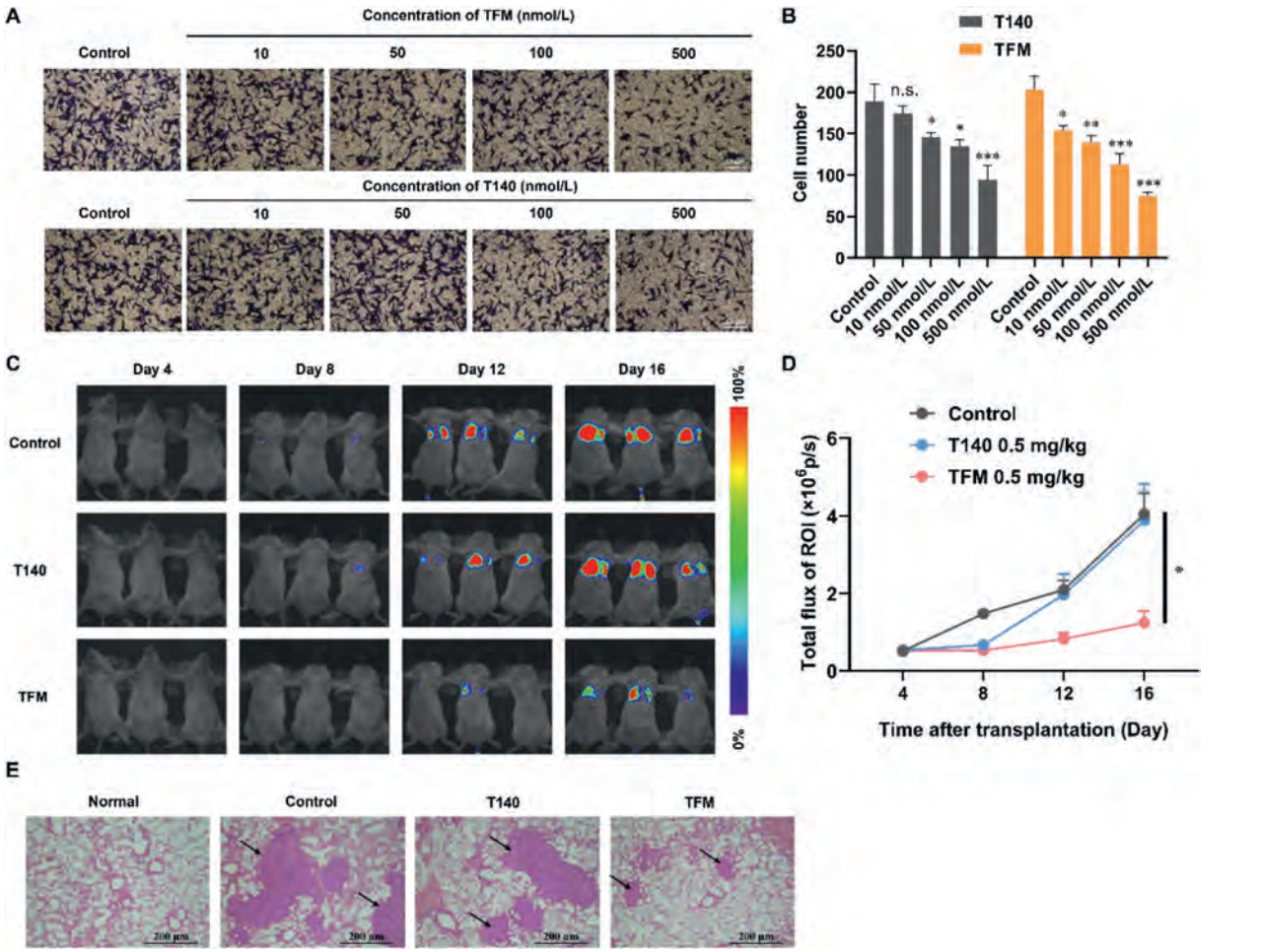

Figure 5 TFM inhibits cancer cell metastasis. (A) Transwell assay of invasion for 4T1 cells treated with T140 or TFM. Scale bar = 50 μm. (B) Quantification of the cells that migrated to the lower chamber. (C) *In vivo* bioluminescence images of mice on Days 4, 8, 12, and 16 after injection of 4T1 cells. (D) Tumor growth curves as determined by quantification analysis of the *in vivo* bioluminescence signal (mean ± SEM, $n = 3$). (E) H&E staining of lung sections (The black arrows indicate metastatic tumors). Scale bar = 200 μm. Data in (B) and (D) were analyzed by one-way ANOVA, $^*P < 0.05$, $^{**}P < 0.01$, $^{***}P < 0.001$. n.s., not significant.

groups were 56.08% and 55.62%, respectively, while the TGI of the TFM and IR combination group was 75.19% (Fig. 6C).

To study the effect of TFM and radiotherapy on the tumor immune microenvironment, we analyzed tumor single-cell suspensions by flow cytometry (Supporting Information Fig. S31). A remarkable increase in the number of $CD8^+$ T cells was observed in the combination therapy group, though there was no significant effect after treatment with either IR or TFM alone (Fig. 6D). Furthermore, combination therapy promoted the secretion of Granzyme B from $CD8^+$ T cells, which is indicative of increased cytotoxicity to tumor cells (Fig. 6E). Both TFM and the combination therapy reduced the proportion of myeloid-derived suppressor cells (MDSCs) and regulatory T cells (Tregs) in the tumors, but IR alone had minimal effect on the proportions of these immunosuppressive cells (Fig. 6F and G). There was also no significant effect on body weight in any of the groups (Fig. 6H) and no obvious toxicity to the liver or kidney according to blood biochemical analysis (Fig. 6I–L and Supporting Information Fig. S32A–S32D). Besides, to figure out the mechanism of $CD8^+$ T cell infiltration and activation induced by TFM, we investigated the effect of TFM on immune cell death (ICD) of 4T1 cells and verified that TFM can cause exposure of calreticulin (CRT), ATP secretion and the release of high mobility group box 1 (HMGB1) (Supporting Information Fig. S33A–S33C). Taken together, these results indicate that the combination of IR and TFM inhibits tumor progression, which is associated with increased tumor $CD8^+$ T cell infiltration and granzyme secretion and reduced proportions of immunosuppressive MDSCs and Tregs.

Next, we investigated whether TFM can inhibit the growth of tumors derived from B16F10, a rapidly growing murine melanoma cell line that expresses both CXCR4 and FOLR1. Strikingly, TFM inhibited the growth of B16F10 tumors with a TGI of

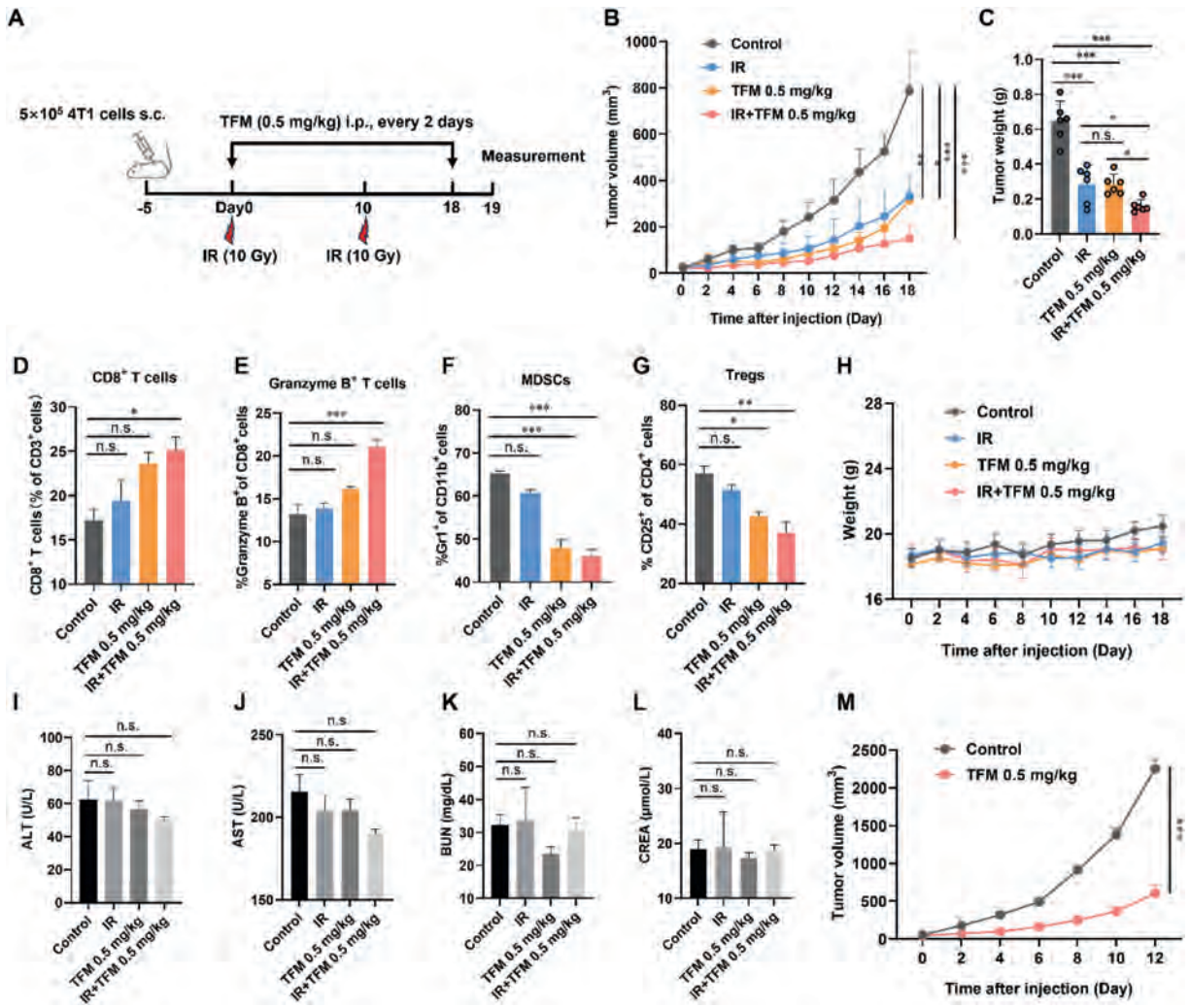

Figure 6 Combination of TFM with irradiation synergistically inhibits tumor growth. (A) Schematic diagram of TFM and irradiation (IR) combination therapy in the 4T1 tumor model. (B) Tumor growth curve of 4T1 tumor-bearing mice treated with saline, IR, TFM, or TFM and IR in combination (mean ± SEM, $n = 6$). (C) Statistical analysis of tumor weights between different groups (mean ± SEM, $n = 6$). (D–G) Changes in the population of $CD3^+$ $CD8^+$ T cells (mean ± SEM, $n = 3$) (D), $CD8^+$ Granzyme B^+ T cells (means ± SEM; $n = 3$) (E), $Gr1^+$ $CD11b^+$ cells (MDSCs) (means ± SEM; $n = 3$) (F), $CD4^+$ $CD25^+$ cells (Tregs) (means ± SEM; $n = 3$) (G). (H) Body weight change of 4T1 tumor-bearing mice. (I–L) Serum biochemical index for ALT (I), AST (J), BUN (K) and CREA (L). (M) Tumor growth curve of B16F10 tumor-bearing mice treated with saline and TFM. Data in (B), (C), (D–G) and (I–M) were analyzed by one-way ANOVA, $^*P < 0.05$, $^{**}P < 0.01$, $^{***}P < 0.001$. n.s., not significant.

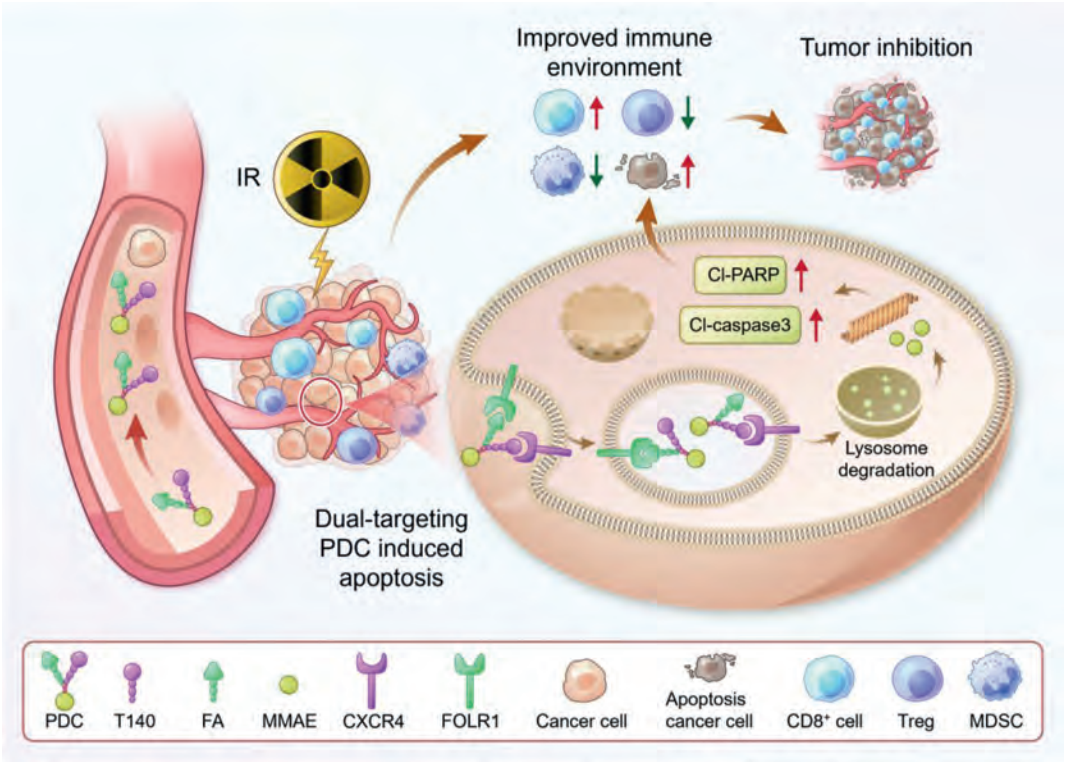

Figure 7 The combination of TFM and irradiation synergistically induces immunogenic cell death in TNBC cells and improves the immune environment. A schematic diagram presenting the key findings of the study demonstrates the impact of combination therapy on TNBC tumor growth by promoting apoptosis, increasing the $CD8^+$ cell infiltration, and reducing the proportion of immunosuppressive cells.

64.22% (Fig. 6M, Supporting Information Fig. S34A, S34C and S34D) and no influence on body weight (Fig. S34B). These results suggest that TFM can target a variety of types of tumors expressing CXCR4 and FOLR1, indicating that its applicability may extend beyond TNBC.

4. Discussion

Despite the emergence of advanced therapeutics in modern oncology, such as targeted therapies and immunotherapies, cytotoxic chemotherapy remains the first-line treatment for TNBC. However, the non-specific targeting and unwanted accumulation of systemically delivered drugs in various organs can cause serious toxicity. Many efforts have been made to overcome the toxicity of chemotherapy drugs by improving their delivery to tumors, with active targeting of tumors being one of the most popular approaches. Nevertheless, this approach has been challenged by intra-tumor heterogeneity and a lack of effective molecular targets in TNBC[10]. Therefore, a delivery vector capable of promoting local apoptotic cell death and inducing systemic cytotoxic responses based on T cells is needed for TNBC treatment.

In this study, we provided a dual-targeting PDC (TFM) that combines T140 and FA, targeting both CXCR4 and FOLR1, each of which is highly expressed on the surface of breast cancer cells. We demonstrated that the binding of either T140 or FA to receptors stimulates the internalization of the PDC into tumor cells and lysosomal localization, which facilitates linker cleavage by cathepsin B, thereby mediating MMAE release. We demonstrated significant activity of TFM against tumors expressing CXCR4 and FOLR1 and observed prolonged retention of a radiolabeled derivative of TFM, [^{64}Cu]TFD, in tumors using PET imaging. The latter results indicate that PRCs can serve as a valuable tool for directing the development of PDCs, and the combination of TFD (PRC) and TFM (PDC) may provide a comprehensive approach to effective cancer theranostics. In the treatment of MDA-MB-231 xenografts with high expression of both CXCR4 and FOLR1, TFM promoted tumor regression, while higher doses of PTX had limited growth retardation. These animal experiments indicate that TFM is a promising targeted treatment strategy for TNBC tumors.

Tumor metastasis is an important consequence of malignant transformation and cancer progression, and it is also the main reason for treatment failure[47]. CXCR4 is often highly expressed on the surface of tumor cells with greater metastasis potential, which is influenced by CXCL12 to metastasize[48]. In our study, we compared the antitumor cell metastasis effects of TFM (targeting CXCR4 and FOLR1) and T140 (targeting CXCR4 alone), which we evaluated both *in vitro* and *in vivo*. T140 and TFM each promoted inhibition of 4T1 cell migration in Transwell experiments. However, in the lung metastasis model, T140 failed to inhibit the metastasis and growth of 4T1 cells in the lungs of mice, while TFM effectively controlled the colonization of 4T1 in cells. Therefore, TFM can recognize highly metastatic TNBC cells and cause apoptosis, thus effectively inhibiting tumor metastasis in normal organs.

Radiotherapy can directly induce tumor cell death *via* apoptosis, necrosis, autophagy, or other mechanisms. However, some tumors are not sensitive to radiation therapy, resulting in poor efficacy and high recurrence rates. Combination therapy, including double, triple, or even quadruple treatment, has shown excellent and durable efficacy[49]. According to our experimental

results, the combination of TFM and IR can effectively control tumor growth, which is accompanied by 1) $CD8^+$ T cell infiltration and activation and 2) depletion of immunosuppressive cells (Fig. 7). Importantly, TFM can maximize the benefits of IR and reduce the systemic toxicity. Immunotherapy provides an additional promising alternative for treating refractory solid tumors that are resistant to chemotherapy, including heterogeneous tumors[50], and targeting of the CXCL12/CXCR4 axis has recently been proposed as a potential strategy for tumors that are resistant to immunotherapy[51,52]. Therefore, it would be worth evaluating the PDCs in combination with immunotherapy.

As a limitation, these results were generated using human cell lines and mouse models. Although we achieved impressive results in mouse models, these findings cannot be directly translated to humans due to species differences. Accurate determination of the optimal doses of IR and PDC, as well as the potential side effects, such as immune-related adverse events, is crucial.

In summary, TFM can induce regression of TNBC xenografts with high expression of CXCR4 and FOLR1 in several mouse models. Furthermore, TFM can cooperate with IR to induce primary tumor apoptosis and improve the immune microenvironment, thereby leading to durable TNBC tumor suppression. TFM can also inhibit the colonization and growth of metastatic TNBC cells in normal organs *via* targeting and killing of cancer cells expressing CXCR4. The excellent antitumor activity and prominent immuno-enhancement efficacy indicate that TFM has the potential to be a therapeutic formulation for TNBC treatment.

Acknowledgments

This study was supported by the Program for the Ministry of Education "Peptide Drugs" Innovation Team (No. IRT_15R27, China), the CAMS Innovation Fund for Medical Sciences (CIFMS, Nos. 2019-I2M-5-074, 2021-I2M-1-026, 2021-I2M-3-001, 2022-I2M-2-002, and 2023-I2M-QJ-010, China), the Fundamental Research Funds for the Central Universities (No. lzujbky-2023-11, China), and the Key Research and Development Program of Gansu Province (23YFFA0047, China).

Author contribution

Kun Wang: Writing − original draft, Validation, Resources, Methodology, Formal analysis, Data curation, Conceptualization. Cong Wang: Validation, Methodology, Data curation. Hange Yang: Methodology, Formal analysis, Data curation. Gong Chen: Methodology, Data curation. Ke Wang: Methodology, Data curation. Peihong Ji: Methodology. Xudong Sun: Validation. Xuegong Fan: Data curation. Jie Ma: Visualization. Zhencun Cui: Visualization. Xingkai Wang: Visualization. Hao Tian: Visualization. Dengfu Wu: Visualization. Lu Wang: Visualization. Zhimin Wang: Visualization. Jiangyan Liu: Visualization. Juan Yi: Writing − review & editing, Supervision, Investigation. Kuan Hu: Writing − review & editing, Visualization, Supervision. Hailong Zhang: Writing − review & editing, Writing − original draft, Supervision, Project administration, Investigation, Formal analysis, Conceptualization. Rui Wang: Writing − review & editing, Supervision, Funding acquisition, Conceptualization.

Conflicts of interest

The authors have no conflicts of interest to declare.

Appendix A. Supporting information

Supporting information to this article can be found online at https://doi.org/10.1016/j.apsb.2025.06.012.

References

1. Bodai BI, Tuso P. Breast cancer survivorship: a comprehensive review of long-term medical issues and lifestyle recommendations. *Perm J* 2015;**19**:48−79.
2. Giaquinto AN, Sung H, Miller KD, Kramer JL, Newman LA, Minihan A, et al. Breast cancer statistics, 2022. *CA Cancer J Clin* 2022;**72**:524−41.
3. Siegel RL, Miller KD, Wagle NS, Jemal A. Cancer statistics, 2023. *CA Cancer J Clin* 2023;**73**:17−48.
4. Yi M, Li T, Niu M, Luo S, Chu Q, Wu K. Epidemiological trends of women's cancers from 1990 to 2019 at the global, regional, and national levels: a population-based study. *Biomark Res* 2021;**9**:55.
5. Goldhirsch A, Winer EP, Coates AS, Gelber RD, Piccart-Gebhart M, Thürlimann B, et al. Personalizing the treatment of women with early breast cancer: highlights of the St Gallen international expert consensus on the primary therapy of early breast cancer 2013. *Ann Oncol* 2013;**24**:2206−23.
6. Lin NU, Vanderplas A, Hughes ME, Theriault RL, Edge SB, Wong YN, et al. Clinicopathologic features, patterns of recurrence, and survival among women with triple-negative breast cancer in the National Comprehensive Cancer Network. *Cancer* 2012;**118**:5463−72.
7. Cortes J, Rugo HS, Cescon DW, Im SA, Yusof MM, Gallardo C, et al. Pembrolizumab plus chemotherapy in advanced triple-negative breast cancer. *N Engl J Med* 2022;**387**:217−26.
8. Bardia A, Hurvitz SA, Tolaney SM, Loirat D, Punie K, Oliveira M, et al. Sacituzumab Govitecan in metastatic triple-negative breast cancer. *N Engl J Med* 2021;**384**:1529−41.
9. Swain SM, Shastry M, Hamilton E. Targeting HER2-positive breast cancer: advances and future directions. *Nat Rev Drug Discov* 2023;**22**:101−26.
10. Li Y, Zhang H, Merkher Y, Chen L, Liu N, Leonov S, et al. Recent advances in therapeutic strategies for triple-negative breast cancer. *J Hematol Oncol* 2022;**15**:121.
11. Chen YF, Xu YY, Shao ZM, Yu KD. Resistance to antibody-drug conjugates in breast cancer: mechanisms and solutions. *Cancer Commun* 2023;**43**:297−337.
12. Shi K, Wang G, Pei J, Zhang J, Wang J, Ouyang L, et al. Emerging strategies to overcome resistance to third-generation EGFR inhibitors. *J Hematol Oncol* 2022;**15**:94.
13. Garrido-Castro AC, Lin NU, Polyak K. Insights into molecular classifications of triple-negative breast cancer: improving patient selection for treatment. *Cancer Discov* 2019;**9**:176−98.
14. Leon-Ferre RA, Goetz MP. Advances in systemic therapies for triple negative breast cancer. *Br Med J* 2023;**381**:e071674.
15. Kumar H, Gupta NV, Jain R, Madhunapantula SV, Babu CS, Kesharwani SS, et al. A review of biological targets and therapeutic approaches in the management of triple-negative breast cancer. *J Adv Res* 2023;**54**:271−92.
16. Dumontet C, Reichert JM, Senter PD, Lambert JM, Beck A. Antibody-drug conjugates come of age in oncology. *Nat Rev Drug Discov* 2023;**22**:641−61.
17. Cooper BM, Iegre J, Dh OD, Ölwegård Halvarsson M, Spring DR. Peptides as a platform for targeted therapeutics for cancer: peptide-drug conjugates (PDCs). *Chem Soc Rev* 2021;**50**:1480−94.

18. Fu C, Yu L, Miao Y, Liu X, Yu Z, Wei M. Peptide-drug conjugates (PDCs): a novel trend of research and development on targeted therapy, hype or hope? *Acta Pharm Sin B* 2023;**13**:498−516.
19. Dean TT, Jelú-Reyes J, Allen AC, Moore TW. Peptide-drug conjugates: an emerging direction for the next generation of peptide therapeutics. *J Med Chem* 2024;**67**:1641−61.
20. Das S, Al-Toubah T, El-Haddad G, Strosberg J. (177)Lu-DOTATATE for the treatment of gastroenteropancreatic neuroendocrine tumors. *Expet Rev Gastroenterol Hepatol* 2019;**13**:1023−31.
21. Scala S, Ottaiano A, Ascierto PA, Cavalli M, Simeone E, Giuliano P, et al. Expression of CXCR4 predicts poor prognosis in patients with malignant melanoma. *Clin Cancer Res* 2005;**11**:1835−41.
22. Bian XW, Yang SX, Chen JH, Ping YF, Zhou XD, Wang QL, et al. Preferential expression of chemokine receptor CXCR4 by highly malignant human gliomas and its association with poor patient survival. *Neurosurgery* 2007;**61**:570−9.
23. Lin Q, Fang X, Liang G, Luo Q, Cen Y, Shi Y, et al. Silencing CTNND1 mediates triple-negative breast cancer bone metastasis *via* upregulating CXCR4/CXCL12 axis and neutrophils infiltration in bone. *Cancers (Basel)* 2021;**13**:5703.
24. Zou W, Machelon V, Coulomb-L'Hermin A, Borvak J, Nome F, Isaeva T, et al. Stromal-derived factor-1 in human tumors recruits and alters the function of plasmacytoid precursor dendritic cells. *Nat Med* 2001;**7**:1339−46.
25. Onoue T, Uchida D, Begum NM, Tomizuka Y, Yoshida H, Sato M. Epithelial-mesenchymal transition induced by the stromal cell-derived factor-1/CXCR4 system in oral squamous cell carcinoma cells. *Int J Oncol* 2006;**29**:1133−8.
26. Kajiyama H, Shibata K, Terauchi M, Ino K, Nawa A, Kikkawa F. Involvement of SDF-1alpha/CXCR4 axis in the enhanced peritoneal metastasis of epithelial ovarian carcinoma. *Int J Cancer* 2008;**122**:91−9.
27. Gangadhar T, Nandi S, Salgia R. The role of chemokine receptor CXCR4 in lung cancer. *Cancer Biol Ther* 2010;**9**:409−16.
28. Xu TP, Shen H, Liu LX, Shu YQ. The impact of chemokine receptor CXCR4 on breast cancer prognosis: a meta-analysis. *Cancer Epidemiol* 2013;**37**:725−31.
29. Gupta N, Mohan CD, Shanmugam MK, Jung YY, Chinnathambi A, Alharbi SA, et al. CXCR4 expression is elevated in TNBC patient derived samples and *Z*-guggulsterone abrogates tumor progression by targeting CXCL12/CXCR4 signaling axis in preclinical breast cancer model. *Environ Res* 2023;**232**:116335.
30. Tamamura H, Xu Y, Hattori T, Zhang X, Arakaki R, Kanbara K, et al. A low-molecular-weight inhibitor against the chemokine receptor CXCR4: a strong anti-HIV peptide T140. *Biochem Biophys Res Commun* 1998;**253**:877−82.
31. Masuda R, Oishi S, Tanahara N, Ohno H, Hirasawa A, Tsujimoto G, et al. Paradoxical downregulation of CXC chemokine receptor 4 induced by polyphemusin II-derived antagonists. *Bioconjug Chem* 2012;**23**:1259−65.
32. Beider K, Begin M, Abraham M, Wald H, Weiss ID, Wald O, et al. CXCR4 antagonist 4F-benzoyl-TN14003 inhibits leukemia and multiple myeloma tumor growth. *Exp Hematol* 2011;**39**:282−92.
33. Chowdhuri AR, Laha D, Chandra S, Karmakar P, Sahu SK. Synthesis of multifunctional upconversion NMOFs for targeted antitumor drug delivery and imaging in triple negative breast cancer cells. *Chem Eng J* 2017;**319**:200−11.
34. Wang HC, Huo YN, Lee WS. Folic acid prevents the progesterone-promoted proliferation and migration in breast cancer cell lines. *Eur J Nutr* 2020;**59**:2333−44.
35. Jain A, Fournier PGJ, Mendoza-Lavaniegos V, Sengar P, Guerra-Olvera FM, Iñiguez E, et al. Functionalized rare earth-doped nanoparticles for breast cancer nanodiagnostic using fluorescence and CT imaging. *J Nanobiotechnol* 2018;**16**:26.
36. Moharil P, Wan Z, Pardeshi A, Li J, Huang H, Luo Z, et al. Engineering a folic acid-decorated ultrasmall gemcitabine nanocarrier for breast cancer therapy: dual targeting of tumor cells and tumor-associated macrophages. *Acta Pharm Sin B* 2022;**12**:1148−62.
37. Wei M, Bai J, Shen X, Lou K, Gao Y, Lv R, et al. Glutathione-exhausting nanoprobes for NIR-II fluorescence imaging-guided surgery and boosting radiation therapy efficacy *via* ferroptosis in breast cancer. *ACS Nano* 2023;**17**:11345−61.
38. Epidermoid anal cancer: results from the UKCCCR randomised trial of radiotherapy alone *versus* radiotherapy, 5-fluorouracil, and mitomycin. UKCCCR Anal Cancer Trial Working Party. UK Co-ordinating Committee on Cancer Research. *Lancet* 1996;**348**:1049−54.
39. Morris M, Eifel PJ, Lu J, Grigsby PW, Levenback C, Stevens RE, et al. Pelvic radiation with concurrent chemotherapy compared with pelvic and para-aortic radiation for high-risk cervical cancer. *N Engl J Med* 1999;**340**:1137−43.
40. Macdonald JS, Smalley SR, Benedetti J, Hundahl SA, Estes NC, Stemmermann GN, et al. Chemoradiotherapy after surgery compared with surgery alone for adenocarcinoma of the stomach or gastroesophageal junction. *N Engl J Med* 2001;**345**:725−30.
41. Bisbal Lopez L, Ravazza D, Bocci M, Zana A, Principi L, Dakhel Plaza S, et al. *Ex vivo* mass spectrometry-based biodistribution analysis of an antibody-resiquimod conjugate bearing a protease-cleavable and acid-labile linker. *Front Pharmacol* 2023;**14**:1320524.
42. Bordeau BM, Nguyen TD, Polli JR, Chen P, Balthasar JP. Payload-binding Fab fragments increase the therapeutic index of MMAE antibody−drug conjugates. *Mol Cancer Therapeut* 2023;**22**:459−70.
43. Kuil J, Buckle T, van Leeuwen FW. Imaging agents for the chemokine receptor 4 (CXCR4). *Chem Soc Rev* 2012;**41**:5239−61.
44. Wu B, Chien EY, Mol CD, Fenalti G, Liu W, Katritch V, et al. Structures of the CXCR4 chemokine GPCR with small-molecule and cyclic peptide antagonists. *Science* 2010;**330**:1066−71.
45. Machulkin AE, Uspenskaya AA, Zyk NU, Nimenko EA, Ber AP, Petrov SA, et al. Synthesis, characterization, and preclinical evaluation of a small-molecule prostate-specific membrane antigen-targeted monomethyl auristatin E conjugate. *J Med Chem* 2021;**64**:17123−45.
46. Buckel L, Savariar EN, Crisp JL, Jones KA, Hicks AM, Scanderbeg DJ, et al. Tumor radiosensitization by monomethyl auristatin E: mechanism of action and targeted delivery. *Cancer Res* 2015;**75**:1376−87.
47. Gerstberger S, Jiang Q, Ganesh K. Metastasis. *Cell* 2023;**186**:1564−79.
48. Liu S, Xie SM, Liu W, Gagea M, Hanker AB, Nguyen N, et al. Targeting CXCR4 abrogates resistance to trastuzumab by blocking cell cycle progression and synergizes with docetaxel in breast cancer treatment. *Breast Cancer Res* 2023;**25**:62.
49. Guo S, Yao Y, Tang Y, Xin Z, Wu D, Ni C, et al. Radiation-induced tumor immune microenvironments and potential targets for combination therapy. *Signal Transduct Targeted Ther* 2023;**8**:205.
50. Liu Y, Hu Y, Xue J, Li J, Yi J, Bu J, et al. Advances in immunotherapy for triple-negative breast cancer. *Mol Cancer* 2023;**22**:145.
51. Zhou W, Guo S, Liu M, Burow ME, Wang G. Targeting CXCL12/CXCR4 axis in tumor immunotherapy. *Curr Med Chem* 2019;**26**:3026−41.
52. Mezzapelle R, Leo M, Caprioglio F, Colley LS, Lamarca A, Sabatino L, et al. CXCR4/CXCL12 activities in the tumor microenvironment and implications for tumor immunotherapy. *Cancers (Basel)* 2022;**14**.